



Mechanical modulation of terahertz wave via buckled carbon nanotube sheets

SHI-TONG XU,^{1,6} LIN-LIN MOU,^{2,6} FEI FAN,^{1,3,*} SAI CHEN,^{1,4} ZHIKAI ZHAO,¹ DONG XIANG,¹ MÔNICA JUNG DE ANDRADE,⁵ ZUNFENG LIU,^{2,7} AND SHENG-JIANG CHANG¹

¹Institute of Modern Optics, Nankai University, Tianjin 300071, China

²State Key Laboratory of Medicinal Chemical Biology, College of Pharmacy, Nankai University, Tianjin 300071, China

³State Key Laboratory of Applied Optics, Changchun Institute of Optics, Fine Mechanics and Physics, Chinese Academy of Sciences, Changchun 130033, China

⁴Nanophotonics and Optoelectronics Research Center, Qian Xuesen Laboratory of Space Technology, China Academy of Space Technology, Beijing 100094, China

⁵Alan G. MacDiarmid NanoTech Institute, University of Texas at Dallas, Richardson, TX 75080, USA

⁶These authors equally contribute to this paper

⁷liuzunfeng@nankai.edu.cn

*fanfei_gdz@126.com

Abstract: Manipulation of terahertz (THz) wave plays an important role in THz imaging, communication, and detection. The difficulty in manipulating the THz wave includes single function, untunable, and inconvenient integration. Here, we present a mechanically tunable THz polarizer by using stretchable buckled carbon nanotube sheets on natural rubber substrate (BCNTS/rubber). The transmittance and degree of polarization of THz wave can be modulated by stretching the BCNTS/rubber. The experiments showed that the degree of polarization increased from 17% to 97%, and the modulation depth reached 365% in the range of 0.2-1.2 THz, as the BCNTS/rubber was stretched from 0% to 150% strain. These changes can be also used for high strain sensing up to 150% strain, with a maximum sensitivity of 2.5 M/S. A spatial modulation of THz imaging was also realized by stretching and rotating BCNTS/rubber. The theoretical analysis and numerical modeling further confirm the BCNTS/rubber changes from weak anisotropic to highly anisotropic structure, which play key roles in THz wave modulation. This approach for active THz wave manipulation can be widely used in polarization imaging, wearable material for security, and highly sensitive strain sensing.

© 2018 Optical Society of America under the terms of the [OSA Open Access Publishing Agreement](#)

1. Introduction

Terahertz (THz) radiation defines as the electromagnetic wave within the frequency range from 0.1 to 10 THz [1,2]. In recent years, great progress in THz generation, detection, and manipulation have enabled these techniques with diverse applications including THz imaging for security and biology [3,4], wireless communications [5,6] spectral detection and strain sensing [7,8]. However, the manipulation components for THz waves are still in the primitive stage of development, such as polarizers [9,10], modulators and switches [11,12], phase shifters [13,14] and sensors [15,16]. In particular, polarizer is a fundamental optical element and could detect and control the polarization state of THz wave. Nowadays, active modulation of polarization and phase for THz wave are attracting great interest, because of the demands in polarization communication, polarization imaging, and polarization spectroscopy [17,18]. Traditional metal wire grid polarizers show excellent polarizing performance in detection or generation of linear polarized THz wave [19,20], but they could not be used for active modulation of THz wave because of their rigidity and non-tunable structures.

Recently great progress have been achieved by using different materials and design in active manipulation of THz wave, including graphene and liquid crystals using gate electrode [21],

semiconductor and graphene by pumping light and metamaterials by thermal or mechanical modulation [22]. Mechanical tuning by stretching, winding, and rotating are effective ways to realize active modulation of THz wave [23]. At present, the THz active devices via mechanical-stretch ability face major problems such as complex fabrication, low stretch ability, and limited modulation depths. For examples, Li *et al.* proposed a mechanically tunable THz metallic metamaterial on a highly elastic polydimethylsiloxane (PDMS) substrate. Due to the non-stretch and fracture of metallic microstructures, the resonance frequency of metamaterial can be only tuned 8.3% [24]. Pitchappa *et al.* proposed a micro-electromechanical system (MEMS) metamaterial to active THz modulation [25]. Kan *et al.* proposed a THz polarization modulator employing vertically deformable 3D chiral spirals, in which the polarization rotation of 28° can be achieved [26]. However, they are also limited by the complicated fabrication, strong driving electric field, narrow tuning range and bandwidth. More importantly, actively controlling amplitude and polarization of THz wave in a single device or structure at the same time has merely been reported so far, which can be integrated with more functions in one device.

Therefore, materials and strategies for mechanically tunable THz devices are highly demanded to obtain a broader tuning range, wider operating bandwidth, and more functions. Carbon nanotubes (CNT), especially super-aligned carbon nanotube sheets (SACNTS) formed by parallel arrays of CNT, have unique ultra-broadband anisotropic optical properties [27–29]. In particular, they exhibit essentially excellent polarization anisotropy in the THz regime, ideally suited for THz polarizer applications [30,31]. For examples, Ren *et al.* achieved an ideal polarizer at a broadband with 99.9% polarization degree and extinction ratios of 10^{-3} based on triple-layer single-walled CNT films on sapphire substrates [32]. Kyoung *et al.* reported on a high-performance THz CNT polarizer by mechanically winding SACNTS on a U-shaped polyethylene frame [33]. However, to the best of our knowledge, no THz polarizers based on CNT could be tunable due to the poor stretch ability of CNT itself.

In this paper, we utilized a structure of buckled CNT sheets on the rubber (BCNTS_{*m*}/rubber, *m* represents the number of layers of BCNTS) to withstand large deformations as a tunable THz polarization device. It was fabricated simply by transferring SACNTS on a pre-stretched rubber substrate and then releasing of the pre-strain. The buckled structure gradually disappeared during stretching and appeared again when the substrate was released. Based on this, it can be widely used for active THz wave manipulation, polarization imaging, and strain sensing.

2. Experimental methods

2.1 Device fabrications

The SACNTS used here were drawn from multiwalled CNT (MWCNT) forests (≈ 6 walls, ≈ 9 nm of outer diameter) grown by chemical vapor deposition (CVD). The SACNTS showed good flexibility and toughness, as well as good compatibility with the polymer materials. The BCNTS/rubber was prepared via a prestretch-release process shown in Fig. 1(a). Briefly, an elastic natural rubber sheet (length: 30 mm, width: 15 mm) is uniaxially stretched to 150% strain (called fabrication strain), and then one-layer CNT was stacked onto the pre-strained rubber substrate. The orientation of carbon nanotubes in SACNTS was parallel to the stretch direction of the natural rubber sheet. After uniform coating of SACNTS layer on rubber substrate, ethanol was sprayed on the SACNTS. After evaporation of the ethanol, the SACNTS adhered firmly to the natural rubber. Repeat the above steps, the pre-strain of rubber was then released and the BCNTS_{*m*}/rubber was formed.

Figure 1(b) shows the scanning electron microscopic (SEM) images of BCNTS₂₀/rubber at different strain. The stretch/release direction of the BCNTS₂₀/rubber was along the horizontal direction. Due to the pre-strain and release of rubber substrate, the CNT of BCNTS₂₀/rubber at 150% strain presents well-organized status. By contrast, the parallel buckles were observed apparently in the stretch/release direction at 90% and 30% strain. In addition, as the degree of tension decreases, the more obvious and dense the fold was. Some kinks were observed in the

buckle ridges, and the alignment directions of the CNT in the kinks were distorted compared to other areas. The formation of these kinks should be ascribed to width expansion during release of the pre-strain of the rubber substrate. The thickness of one layer of CNT is 10 nm. In fact, there are some gaps between CNTs in the same layer, so the multi-layer of CNT will make the CNT from adjacent layer to filling the gap. Thus, the total thickness of 20-layer of CNT sheet is slightly less than 200nm. When the stretch is released, the thickness of the sheet will not increase.

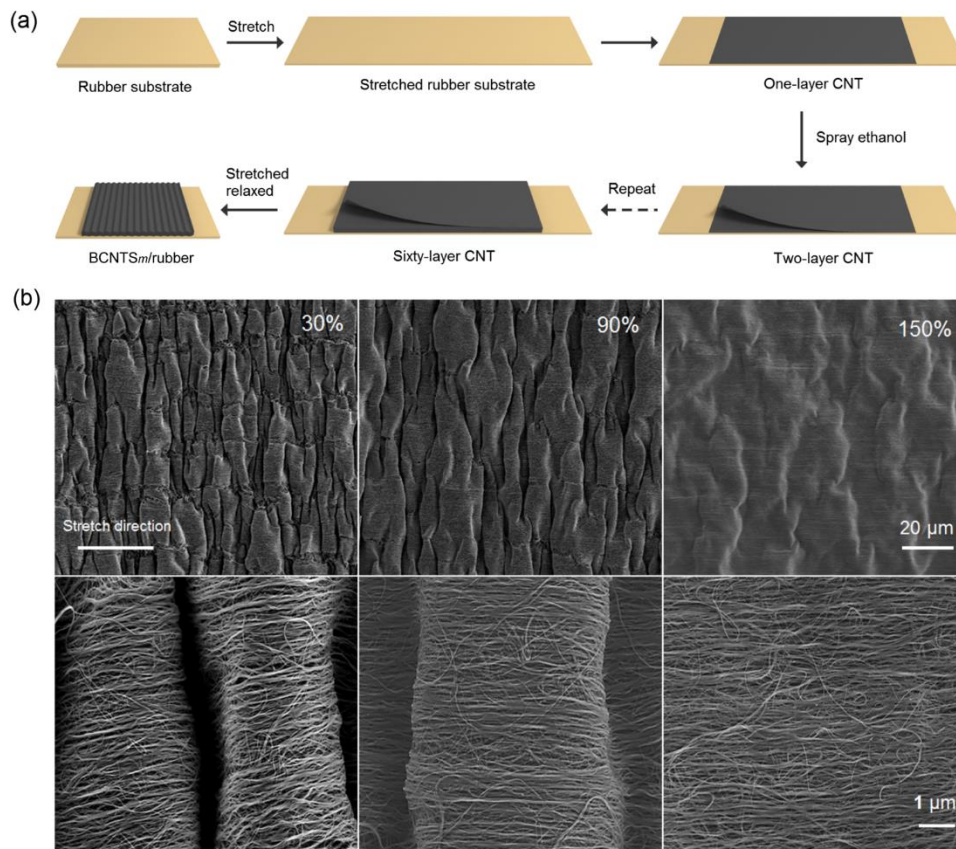


Fig. 1. (a) Schematic illustration of fabrication steps of a BCNTS/rubber. (b) Low- and high-resolution SEM images showing buckles of a BCNTS₂₀/rubber at 30%, 90%, and 150% strain.

2.2 Experimental system

A standard THz time domain spectroscopy (THz-TDS) system was used to conduct the THz experiment, as schematically shown in Fig. 2(a). The THz pulse was generated by a low-temperature grown GaAs photoconductive antenna. The excitation source was a Ti: sapphire laser with 75 fs duration of 80 MHz repetition rate at 800 nm. A ZnTe crystal was used for detection. All the experiments were carried out at room temperature with humidity of less than 5%, and the signal to noise ratio (SNR) of system was more than 50dB from 0.2 to 1.2 THz. The amplitude spectra $A(f)$ can be obtained by doing Fourier transform of the time-domain signal:

$$A(f) = |FFt[E(t)]|, \quad (1)$$

where $E(t)$ is the measured time-domain THz signal from THz-TDS. And the amplitude transmission spectra are calculated by:

$$t(f) = A_s(f)/A_r(f), \quad (2)$$

where $A_s(f)$ and $A_r(f)$ are the amplitude spectra of the sample and air, respectively.

In addition, as shown in Fig. 2(b), it can be seen that the mechanical properties of the rubber substrate showed negligible changed after attaching BCNTS on the rubber substrate, and it has a good mechanical recovery characteristic.

As a control experiment, we firstly tested the THz time-domain spectra of the bare rubber substrate at different strain, as shown in Fig. 2(c). The measured THz time signal moved forward with stretching the rubber substrate, and the amplitude transmission peak stayed at nearly the same level (90% from 0% to 150% strain), which means that only the phase of THz waves was modulated by stretching the rubber substrate. This phase shift during stretching should be ascribed to the decreased optical path because the rubber became thinner during the stretching. During strain increase of the rubber substrate, the intensity and polarization of THz wave were not modulated.

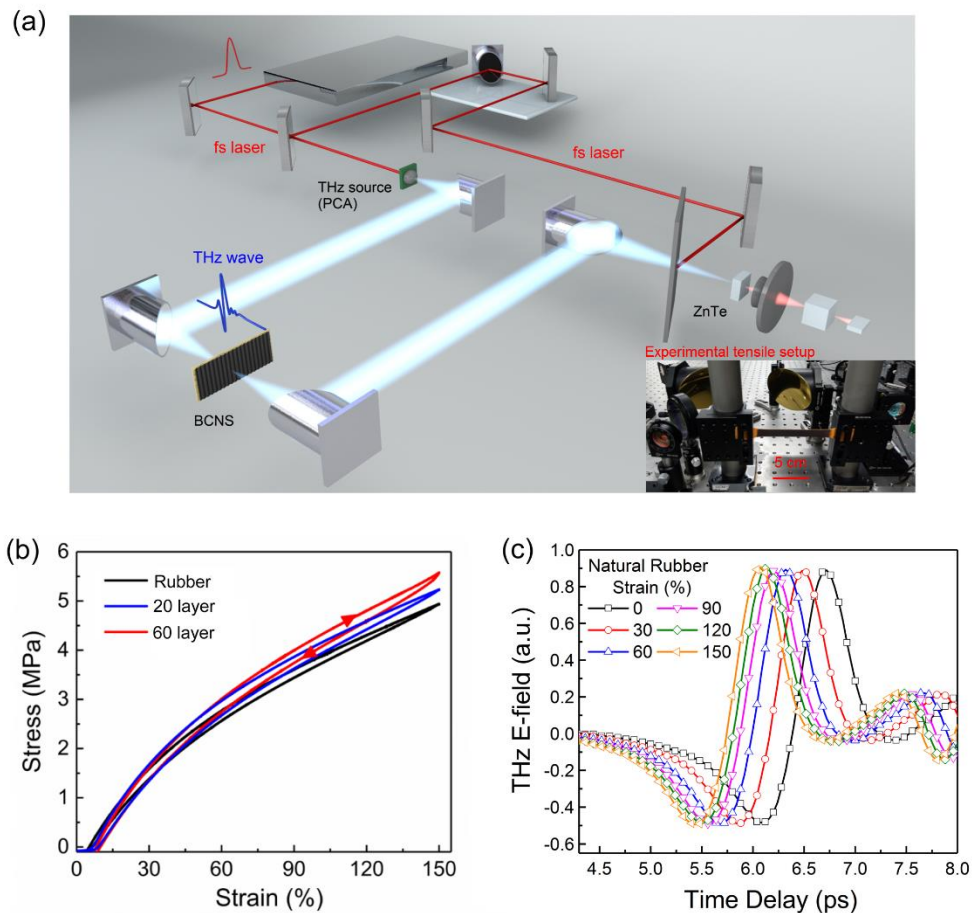


Fig. 2. (a) Schematic diagram of THz-TDS, insets: experimental tensile setup. (b) The stress-strain curve of bare rubber, BCNTS₂₀/rubber, and BCNTS₆₀/rubber. (c) Time-domain THz spectra of bare rubber substrate at different strain 0%, 30%, 60%, 90%, 120% and 150%.

3. Results and discussions

3.1 Tunable polarization characteristics

Next, we analyzed the THz time-domain spectra of the BCNTS/rubber for the cases of BCNTS // THz and BCNTS \perp THz at different strain, as shown in Fig. 3. The polarization angle was defined as the rotating angle of CNT alignment direction to the THz polarization direction, which was 0° in the parallel case (BCNTS // THz) and 90° in the perpendicular case (BCNTS \perp THz). The results of BCNTS₂₀/rubber were shown in Figs. 3(a) and 3(b). On stretching the BCNTS/rubber, the THz time signal moved forward with less time delay, and the peak values increased for BCNTS \perp THz case and decreased for BCNTS // THz with strain increase. The modulation of amplitude transmission and phase of THz wave by stretching BCNTS₆₀/rubber were similar to that of BCNTS₂₀/rubber. This indicates that both amplitude transmission and phase of the THz wave were modulated by stretching the BCNTS/rubber. After doing Fourier transform of time domain signals, the corresponding amplitude transmission can be calculated, respectively.

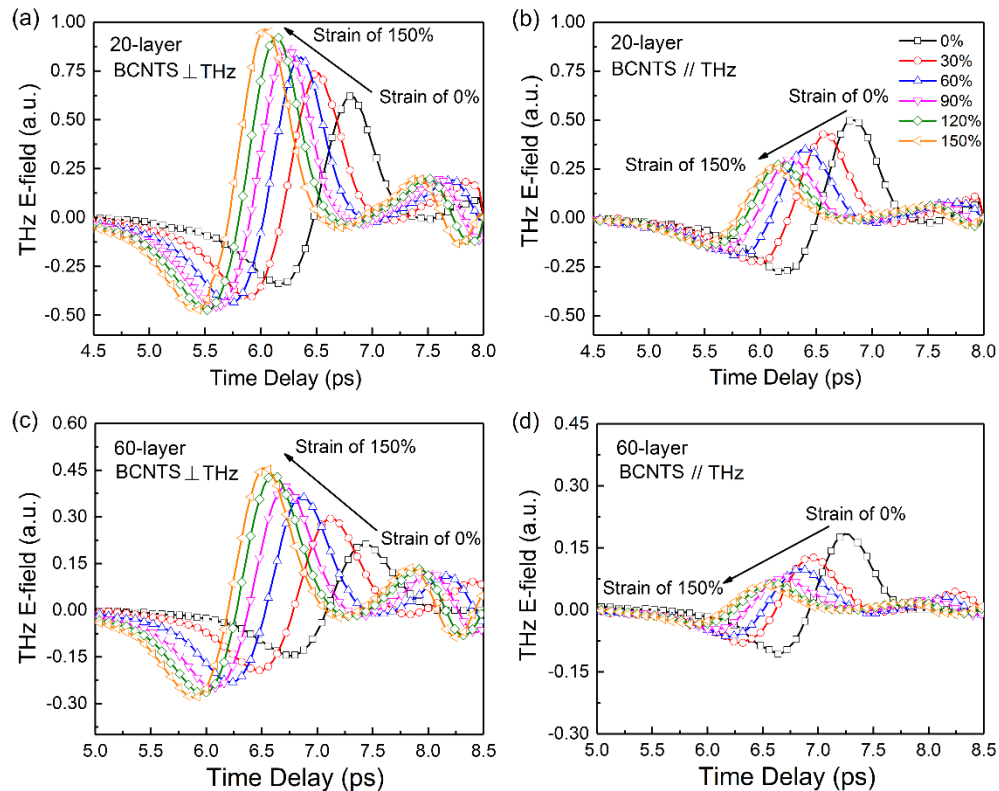


Fig. 3. Time-domain THz waveform for BCNTS/rubber \perp THz and BCNTS/rubber // THz of (a, b) 20-layer and (c, d) 60-layer for strain increasing from 0% to 150%.

The amplitude transmission spectra of BCNTS₂₀/rubber for the BCNTS // THz and BCNTS \perp THz cases with the different strain, as shown in Fig. 4(a). When there is no strain, the amplitude transmission of BCNTS \perp THz is only slightly higher than that of BCNTS // THz, both close to 40% (44.63% and 39.29% at 1 THz, respectively). When the strain increases from 0 to 150%, the amplitude transmission of BCNTS \perp THz increases to 70.67%, but BCNTS // THz inversely drops down to 18.50%. The BCNTS/rubber having other number of layers from 5 to 60 showed similar trends as the BCNTS₂₀/rubber in modulating THz wave, and the results of BCNTS₆₀/rubber are shown in Fig. 4(b), with total amplitude transmission smaller than that of

BCNTS₂₀/rubber. It is obvious that the amplitude transmission of BCNTS/rubber is strongly dependent on the changes of buckled structure, and its THz anisotropic properties can be actively tuned in the stretching process.

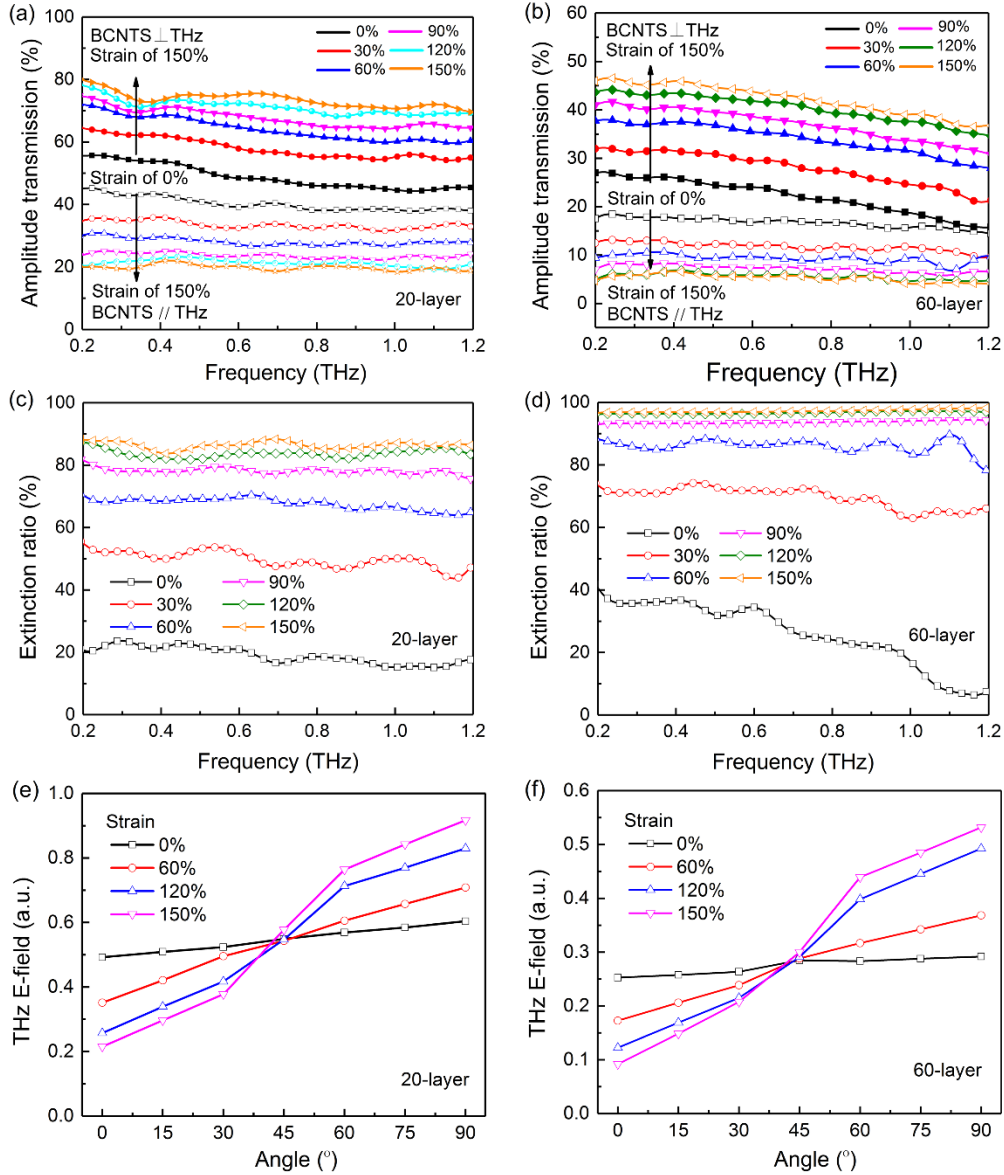


Fig. 4. Amplitude transmission spectra of BCNTS/rubber for the BCNTS // THz and BCNTS ⊥ THz cases of (a) 20-layer and (b) 60-layer with the different strain. Extinction ratio for BCNTS/rubber of (c) 20-layer and (d) 60-layer at the different strain. The peak signal of the Time-domain THz spectra for the (e) 20-layer and (f) 60-layer as a function of polarization angle at different strain.

To study the influence of anisotropic properties of BCNTS/rubber as a tunable THz polarizer, we calculated the extinction ratio (ER) of the THz wave as a function of frequency (f), which was defined as [30,33]:

$$ER(f) = (t_{\perp}^2 - t_{//}^2) / (t_{\perp}^2 + t_{//}^2), \quad (3)$$

where $t_{//}$ and t_{\perp} are the amplitude transmission of THz wave for the cases of BCNTS//THz and BCNTS \perp THz, respectively. The ER is 100% for an ideal polarizer since it creates fully linearly polarized light. Figures 4(c) and 4(d) show the ER of THz wave at 0.2-1.2 THz for BCNTS/rubber at different strain for $m = 20$ and 60, respectively. For BCNTS₂₀/rubber, the ER increased gradually from 16.6% to 88.3% at 1THz when strain increased from 0% to 150%. For BCNTS₆₀/rubber, the ER increased from 17% to 97% at 1THz, and the THz spectra showed negligible dispersion as the strain was larger than 90%. It indicates that higher ER values can be obtained for BCNTS/rubber having a larger number of CNT layers. However, the more layers of CNT, the lower the transmittance it has, as shown in Figs. 4 (a) and 4(b). The results indicate that the BCNTS/rubber can be used as an efficient tunable THz polarizer, which can be changed from a nearly isotropic state at 0% strain to a highly anisotropic state at high strain.

In addition, we studied the THz polarization properties of BCNTS/rubber as a function of polarization angle at different strain as shown in Fig. 4(e). The BCNTS/rubber is fixed on the sample holder that can be rotated by any angles. The input THz wave in THz-TDS system is linearly polarized, and then the relative orientation of incident polarized light and CNT can be realized by rotating the sample holder. The peak of the THz time-domain signal of BCNTS/rubber at 0% strain linearly increased from 39% to 48% as the polarization angle increased from 0° to 90° for $m = 20$. The similar results of $m = 60$ are shown in Fig. 4(f). At higher strains for BCNTS/rubber, the peak increased more prominently with the increase of polarization angle. The peak decreased with strain increase as the polarization angle is smaller than 45°, and increased with strain increase when the polarization angle is higher than 45°, and kept constant at the polarization angle of 45°. Therefore, the BCNTS/rubber at stretched state shows highly anisotropic properties, which can be used as a tunable THz polarizer to control the polarization and amplitude transmission of THz waves.

3.2 Theoretical analysis and simulation

To understand the observed strain-dependent THz amplitude transmission, we characterized the BCNTS₂₀/rubber at different strain by SEM. Figure 1 shows the obvious buckled structure was observed for BCNTS at 30% strain. The distance between buckles got larger as strain increased, and finally the buckles disappeared at strain 150%. In the highly stretched BCNTS/rubber, the CNT was highly aligned in the stretch direction and worked as a conducting wire grating for THz wave. The THz amplitude transmission for BCNTS//THz is low and that for BCNTS \perp THz is high, so the BCNTS/rubber at high strain is an efficient THz polarizer. At low strain, the formation of buckles and kinks in BCNTS/rubber largely broke the anisotropy of CNT in the alignment direction. The THz amplitude transmissions for BCNTS//THz and BCNTS \perp THz are very close to each other, and therefore BCNTS/rubber at low strain served as a nearly isotropic material for THz wave.

A numerical model with a structure of BCNTS grating was used to simulate the THz polarization and modulation behaviors of BCNTS/rubber at different strain, as illustrated in Fig. 5(a). In this model, the BCNTS was statistically taken as a pair of orthogonal optical gratings of CNT. The vertical grating grid represents the CNT alignment direction during fabrication and the pre-stretch direction of the rubber substrate, where b represents the period of this vertical grating. Because there are buckles and defects in the BCNTS/rubber at low strains, the orientation of CNT is partially deteriorated. Therefore, another horizontal grating was used to represent the CNT buckles and defects that are aligned perpendicular to the pre-stretch direction, where a represents the period of this horizontal grating. The geometric parameter c represents the statistical width of the CNT gratings, and it stays the same during stretching.

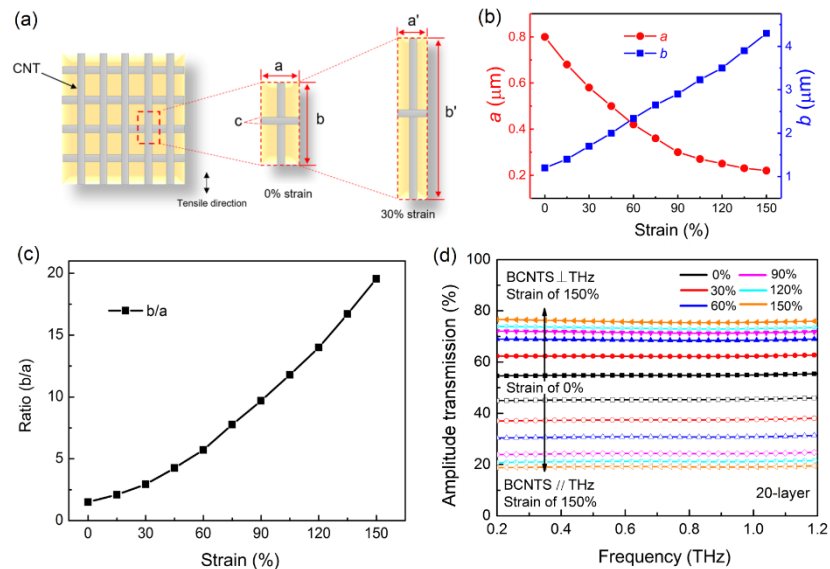


Fig. 5. (a) The diagram of the statistical grating model of BCNTS/rubber, the yellow part represents rubber and the gray wires represent CNT gratings. (b) The simulated values of a and b in (a) as a function of strain. (c) The simulated values of b/a in (a) as a function of strain. (d) The simulated amplitude transmission spectra of BCNTS₂₀/rubber for the cases of BCNTS \perp THz and BCNTS \parallel THz at different strain.

The commercial software Lumerical FDTD Solution was used to make the full-wave electromagnetic field simulation for the above model based on the finite difference time domain (FDTD) method [34]. Here, the CNT gratings exhibit semi-metallic characteristics and it was set as an electrical conductivity of 5×10^5 S/m [35], and the permittivity of rubber was set as 3.09 in the simulation model, which is accurately measured by the THz-TDS system. Only one unit cell is used to describe a pair of periodic orthogonal grating grids as shown in the dotted area of Fig. 5(a), and two pairs of the periodic boundary condition are set. When we set different geometric parameters a , b , and c , the BCNTS/rubber grating model with different strain can be numerically simulated, and the simulated amplitude transmission spectra of BCNTS/rubber for both BCNTS \parallel THz and BCNTS \perp THz cases can be obtained. Although this model looks different from the geometry in Fig. 1(b), it can well indicate the optical properties of BCNTS in the stretching process.

Figure 5(d) shows the simulated amplitude transmission spectra of BCNTS₂₀/rubber with different parameters a and b corresponding to the strain from 0 to 150%. When the strain is 0, both simulated amplitude transmission of BCNTS \perp THz and BCNTS \parallel THz are close to 50%. When the strain increase from 0 to 150%, the amplitude transmission of BCNTS \perp THz increases to >70%, but BCNTS \parallel THz inversely drops down to <20%. All the simulated amplitude transmission spectral curves agree well with the corresponding experimental spectral at different strains shown in Fig. 4(a). Figure 5(b) records the changes of parameters a and b in the simulation process. During stretch of BCNTS/rubber from 0% strain, c keeps constant, a decrease, b increases, which is consistent with the actual situation shown in Fig. 1(b). The parameter b/a represents the geometric asymmetry of BCNTS/rubber, which increases from 2 to 20 as strain increases from 0 to 150%, as shown in Fig. 5(c). This indicates that the BCNTS/rubber changes from weak anisotropic to highly anisotropic structures for THz wave modulation. The numerical simulation results confirm the THz-TDS experiment of BCNTS/rubber, and explain the THz anisotropy and modulation behaviors of BCNTS/rubber during the stretching process. Based on the numerical model that we proposed, the simulated results of 60-layer also can be obtained. The specific value of a , b , and c may change, but the

trend of b/a still increase with the degree of tension. Due to the higher extinction ratio of 60-layer, the maximum value of b/a will greater than 20-layer. In addition, the conductivity of 60-layer is greater than 20-layer.

3.3 Modulation and sensing characteristics

We next discuss the modulation of THz intensity by the BCNTS/rubber and its strain sensing behavior. The intensity modulation depth (MD) is defined as:

$$MD(f) = [t_{\varepsilon}(f)^2 - t_0(f)^2] / t_0(f)^2, \quad (4)$$

where $t_{\varepsilon}(f)$ and $t_0(f)$ are the amplitude transmittance at strain ε % and 0%, respectively. The modulation depth of BCNTS/rubber as a function of strain at 1 THz for different m is shown in Fig. 6(a). It can be seen that the MD of BCNTS/rubber at BCNTS \perp THz is much higher than that at BCNTS \parallel THz for the same number of layers of BCNTS and at the same strain. The MD for both BCNTS \parallel THz and BCNTS \perp THz monotonically increased with increase in the BCNTS layer number and strain, respectively. The maximum MD value of 365% was obtained at 150% strain for BCNTS \perp THz. By comparing Fig. 2(c) and Fig. 3, it can be concluded that phase shifts of BCNTS/rubber come mainly from the thickness change of the rubber substrate.

This performance of MD with strain would make the BCNTS/rubber a good candidate for strain sensing. In order to characterize the strain sensing properties quantitatively, we define the strain sensitivity (SS) as:

$$SS = \partial(MD) / \partial(\varepsilon) \quad (5)$$

which is the derivative of the MD -strain curves shown in Fig. 6(b). The average strain sensitivity of BCNTS/rubber for different m was obtained by fitting of the MD -strain curves. The SS of BCNTS/rubber for BCNTS \perp THz linearly increased from 0.29 to 2.5. The maximum SS value of 2.5 means that, the MD of THz wave changes by 2.5% for per change of strain 1%, indicating a good sensitivity of the strain sensor. The SS of BCNTS/rubber for BCNTS \parallel THz monotonically increased from 0.32 to 0.55 as the number of layers of BCNTS increased from 5 to 60. The stress-strain curves of BCNTS/rubber (for $m = 0, 20$, and 60) are shown in Fig. 2(b), which showed a monotonic change of stress with strain increase. The correlation of stress-strain and the MD -strain would make it a possible way to sense the stress by measuring the MD values.

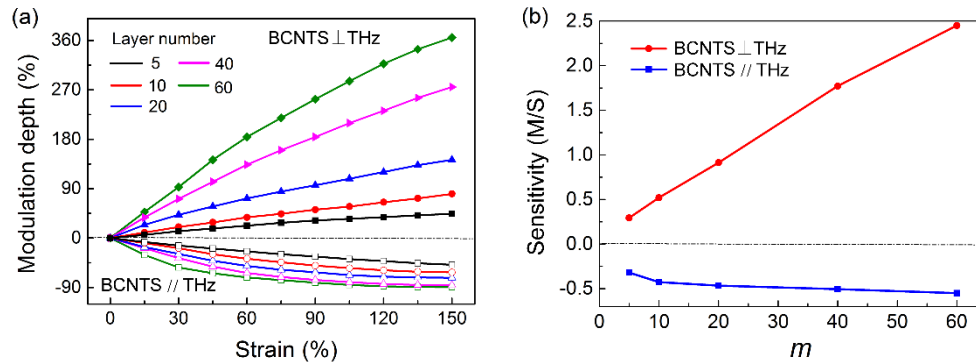


Fig. 6. (a) The modulation depth as a function of strain for BCNTS/rubber with different BCNTS layer number ($m = 5, 10, 20, 40$, and 60, respectively) for the cases of BCNTS \perp THz and BCNTS \parallel THz. (b) Strain sensitivity as a function of number of BCNTS layers for the cases of BCNTS \perp THz and BCNTS \parallel THz.

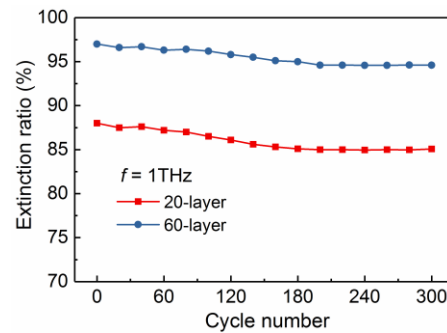


Fig. 7. The extinction ratio curves of BCNTS/rubber at 1THz after different cyclic stretch (red dotted lines represent 20-layer, blue dotted lines represent 60-layer).

In order to illustrate the reliability of BCNTS/rubber after long-time operation, we give the extinction ratio curves of BCNTS/rubber at 1THz with different cycle number, as shown in Fig. 7. On the whole, after many times of stretching, the ER curves have a slight decrease and finally tended to be the same and remain at a high level, which shows that the BCNTS/rubber can withstand multiple operations and maintains the good performance.

3.4 THz polarization imaging

THz imaging has shown the tremendous potential in fields including security screening and biomedical imaging [36–41]. Imaging using THz radiation shows contactless and nondestructive, that is suitable for materials that behind dry and nonpolar materials such as plastics and rubber. Besides the THz imaging, THz shielding is also important for blocking the THz imaging for security and detection requirements [42–45]. For the cases that require switchability and tunability of THz imaging and blocking, we here showed the spatial modulation of THz polarization by using the BCNTS₆₀/rubber, which realized a switchable imaging for a cloaking coin, as shown in Fig. 8(a). Here, the THz wave is generated by an unbiased photoconductive antenna (TD-1550-L165-AR from Eachwave company), which can be stimulated by fs-laser. The sample is placed at the front focal plane of a 4f system made by two THz lenses. The schottky diode detector (3DL-12C-2500LS-A1 from ACST company) is placed at the back focal plane. By 2D scanning at object plane with a motorized precision translation stage, we can detect the intensity transmission of every point from the sample on receiving plane.

The BCNTS₆₀/rubber is clamped on a metal frame with a hole, which can be stretched to different strain and held by the clamp. The metal frame can be rotated with different rotation angle and therefore the orientation of BCNTS can be parallel or perpendicular to the THz polarization direction. We first studied the polarization imaging of the coin by using BCNTS₆₀/rubber for different polarization angles from 0° to 90° at 150% strain, as shown in Fig. 8(b). The coin is hardly seen for the BCNTS//THz case (the polarization angle of 0°), and a circular ring is clearly observed for the case of BCNTS⊥THz (the polarization angle of 90°), with different imaging intensities for the polarization angles in between 0° to 90°. The inner dark circle is the hiding coin and the outside is the metal frame, forming a bright yellow ring for the space between the coin and the metal frame. We then studied the polarization imaging of the BCNTS₆₀/rubber at different strain from 0% and 150% for the case of BCNTS⊥THz, as shown in Fig. 8(c). The coin was hardly seen as the BCNTS₆₀/rubber was at 0% strain, and the intensity of the bright-yellowish circular became clearer by increasing the strain. Therefore, the THz polarization imaging can be tuned by from almost being hidden to being clearly imaged by mechanical stretching or rotating of the BCNTS/rubber. In addition, the single-walled carbon nanotubes (SWCNT) possess higher ER index than MWCNT [30,46]. Therefore, if we

choose the SWCNT instead of MWCNT, the performance of BCNTS in strain sensing and polarization imaging will be further improved.

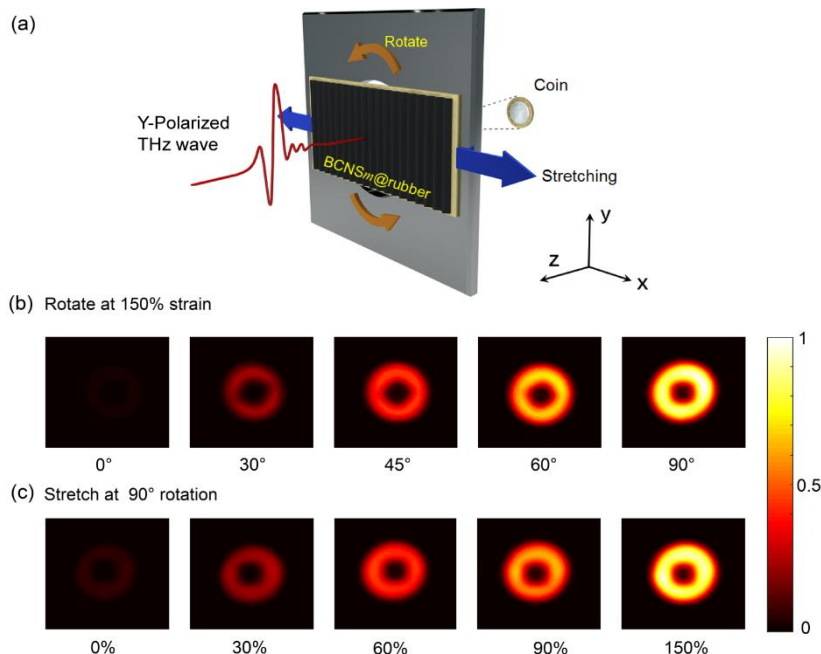


Fig. 8. Tunable THz polarization imaging of a coin by use of BCNTS₆₀/rubber. (a) Schematic demonstration of tunable THz imaging. (b) The THz images with different rotation angle at 150% strain. 0° and 90° are corresponding to the BCNTS₆₀//THz and BCNTS₆₀⊥THz. (c) The THz images at different strain with a rotation angle of 90°.

4. Conclusion

In summary, we fabricated BCNTS/rubber and demonstrated its application in THz polarization modulation, including transmittance and degree of polarization by mechanical stretching, and realized tunable THz polarization imaging by using BCNTS/rubber via rotation and stretching. The change of degree of polarization with strain indicates that the BCNTS/rubber can be used for highly strain sensing. Based on the micro-structural change of the BCNTS/rubber, a grid model was designed and the simulation agreed well with the experimental results. This tunable THz device and its approach for active THz wave manipulation can be widely used in polarization imaging, wearable material for security and high sensitive strain sensing.

Funding

National Key Research and Development Program of China (2017YFA0701000, 2017YFB030700); National Natural Science Foundation of China (61831012, 61671491, 61505088, 51773094, U1533122); Young Elite Scientists Sponsorship Program by Tianjin (TJSQNTJ-2017-12).

References

1. Y.-S. Lee, *Principles of terahertz science and technology*, (Springer Science & Business Media, 2009).
2. B. Ferguson and X. C. Zhang, "Materials for terahertz science and technology," *Nat. Mater.* **1**(1), 26–33 (2002).
3. J. F. Federici, B. Schulkin, F. Huang, D. Gary, R. Barat, F. Oliveira, and D. Zimdars, "THz imaging and sensing for security applications—explosives, weapons and drugs," *Semicond. Sci. Technol.* **20**(7), S266–S280 (2005).
4. G. G. H. Cardoso, S. C. R. Landeros, M. A. Gomez, A. I. Hernandez-Serrano, I. S. Gutierrez, E. L. Bedolla, A. R. C. Guzman, H. L. L. Lemus, and E. C. Camus, "Terahertz imaging for early screening of diabetic foot syndrome: A proof of concept," *Sci. Rep.* **7**, 42124 (2017).

5. T. Nagatsuma, G. Ducournau, and C. C. Renaud, "Advances in terahertz communications accelerated by photonics," *Nat. Photonics* **10**(6), 371–379 (2016).
6. S. Koenig, D. Lopez-Diaz, J. Antes, F. Boes, R. Henneberger, A. Leuther, A. Tessmann, R. Schmogrow, D. Hillerkuss, R. Palmer, T. Zwick, C. Koos, W. Freude, O. Ambacher, J. Leuthold, and I. Kallfass, "Wireless sub-THz communication system with high data rate," *Nat. Photonics* **7**(12), 977–981 (2013).
7. M. Kato, S. R. Tripathi, K. Murate, K. Imayama, and K. Kawase, "Non-destructive drug inspection in covering materials using a terahertz spectral imaging system with injection-seeded terahertz parametric generation and detection," *Opt. Express* **24**(6), 6425–6432 (2016).
8. F. Fan, W.-H. Gu, X.-H. Wang, and S.-J. Chang, "Real-time quantitative terahertz microfluidic sensing based on photonic crystal pillar array," *Appl. Phys. Lett.* **102**(12), 121113 (2013).
9. R.-H. Fan, Y. Zhou, X.-P. Ren, R.-W. Peng, S.-C. Jiang, D.-H. Xu, X. Xiong, X.-R. Huang, and M. Wang, "Freely tunable broadband polarization rotator for terahertz waves," *Adv. Mater.* **27**(7), 1201–1206 (2015).
10. S.-T. Xu, F.-T. Hu, M. Chen, F. Fan, and S.-J. Chang, "Broadband terahertz polarization converter and asymmetric transmission based on coupled dielectric-metal grating," *Ann. Phys.-Berlin* **529**(10), 1700151 (2017).
11. S. Chen, F. Fan, Y. Miao, X. He, K. Zhang, and S. Chang, "Ultrasensitive terahertz modulation by silicon-grown MoS₂ nanosheets," *Nanoscale* **8**(8), 4713–4719 (2016).
12. M. Manjappa, Y. K. Srivastava, L. Cong, I. Al-Naib, and R. Singh, "Active photoswitching of sharp Fano resonances in THz metadevices," *Adv. Mater.* **29**(3), 1603355 (2017).
13. C.-S. Yang, T.-T. Tang, R.-P. Pan, P. Yu, and C.-L. Pan, "Liquid crystal terahertz phase shifters with functional indium-tin-oxide nanostructures for biasing and alignment," *Appl. Phys. Lett.* **104**(14), 141106 (2014).
14. M. Chen, F. Fan, S.-T. Xu, and S.-J. Chang, "Artificial high birefringence in all-dielectric gradient grating for broadband terahertz waves," *Sci. Rep.* **6**(1), 38562 (2016).
15. Y. Zhang, T. Li, B. Zeng, H. Zhang, H. Lv, X. Huang, W. Zhang, and A. K. Azad, "A graphene based tunable terahertz sensor with double Fano resonances," *Nanoscale* **7**(29), 12682–12688 (2015).
16. W. Xu, L. Xie, and Y. Ying, "Mechanisms and applications of terahertz metamaterial sensing: a review," *Nanoscale* **9**(37), 13864–13878 (2017).
17. Z. Miao, Q. Wu, X. Li, Q. He, K. Ding, Z. An, Y. Zhang, and L. Zhou, "Widely tunable terahertz phase modulation with gate-controlled graphene metasurfaces," *Phys. Rev. X* **5**(4), 041027 (2015).
18. Y. Zhang, Y. Feng, T. Jiang, J. Cao, J. Zhao, and B. Zhu, "Tunable broadband polarization rotator in terahertz frequency based on graphene metamaterial," *Carbon* **133**, 170–175 (2018).
19. K. Takano, H. Yokoyama, A. Ichii, I. Morimoto, and M. Hangyo, "Wire-grid polarizer sheet in the terahertz region fabricated by nanoimprint technology," *Opt. Lett.* **36**(14), 2665–2667 (2011).
20. L. Y. Deng, J. H. Teng, L. Zhang, Q. Y. Wu, H. Liu, X. H. Zhang, and S. J. Chua, "Extremely high extinction ratio terahertz broadband polarizer using bilayer subwavelength metal wire-grid structure," *Appl. Phys. Lett.* **101**(1), 011101 (2012).
21. L. Wang, X.-W. Lin, W. Hu, G.-H. Shao, P. Chen, L.-J. Liang, B.-B. Jin, P.-H. Wu, H. Qian, Y.-N. Lu, X. Liang, Z.-G. Zheng, and Y.-Q. Lu, "Broadband tunable liquid crystal terahertz waveplates driven with porous graphene electrodes," *Light Sci. Appl.* **4**(2), e253 (2015).
22. Q.-Y. Wen, W. Tian, Q. Mao, Z. Chen, W.-W. Liu, Q.-H. Yang, M. Sanderson, and H.-W. Zhang, "Graphene based all-optical spatial terahertz modulator," *Sci. Rep.* **4**(1), 7409 (2015).
23. S. Lee, S. Kim, T.-T. Kim, Y. Kim, M. Choi, S. H. Lee, J.-Y. Kim, and B. Min, "Reversibly stretchable and tunable terahertz metamaterials with wrinkled layouts," *Adv. Mater.* **24**(26), 3491–3497 (2012).
24. J. Li, C. M. Shah, W. Withayachumnankul, B. S. Y. Ung, A. Mitchell, S. Sriram, M. Bhaskaran, S. Chang, and D. Abbott, "Mechanically tunable terahertz metamaterials," *Appl. Phys. Lett.* **102**(12), 121101 (2013).
25. P. Pitchappa, M. Manjappa, C. P. Ho, R. Singh, N. Singh, and C. Lee, "Active control of electromagnetically induced transparency analog in terahertz MEMS metamaterial," *Adv. Opt. Mater.* **4**(4), 541–547 (2016).
26. T. Kan, A. Isozaki, N. Kanda, N. Nemoto, K. Konishi, H. Takahashi, M. Kuwata-Gonokami, K. Matsumoto, and I. Shimoyama, "Enantiomeric switching of chiral metamaterial for terahertz polarization modulation employing vertically deformable MEMS spirals," *Nat. Commun.* **6**(1), 8422 (2015).
27. S. Smirnov, I. V. Anoshkin, P. Demchenko, D. Gomon, D. V. Lioubtchenko, M. Khodzitsky, and J. Oberhammer, "Optically controlled dielectric properties of single-walled carbon nanotubes for terahertz wave applications," *Nanoscale* **10**(26), 12291–12296 (2018).
28. I. N. Kholmanov, C. W. Magnuson, R. Piner, J.-Y. Kim, A. E. Aliev, C. Tan, T. Y. Kim, A. A. Zakhidov, G. Sberveglieri, R. H. Baughman, and R. S. Ruoff, "Optical, electrical, and electromechanical properties of hybrid graphene/carbon nanotube films," *Adv. Mater.* **27**(19), 3053–3059 (2015).
29. S. Muhammad, M. Nakano, A. G. Al-Sehemi, Y. Kitagawa, A. Irfan, A. R. Chaudhry, R. Kishi, S. Ito, K. Yoneda, and K. Fukuda, "Role of a singlet diradical character in carbon nanomaterials: a novel hot spot for efficient nonlinear optical materials," *Nanoscale* **8**(42), 17998–18020 (2016).
30. L. Ren, C. L. Pint, T. Arikawa, K. Takeya, I. Kawayama, M. Tonouchi, R. H. Hauge, and J. Kono, "Broadband terahertz polarizers with ideal performance based on aligned carbon nanotube stacks," *Nano Lett.* **12**(2), 787–790 (2012).
31. A. Zubair, D. E. Tsentelovich, C. C. Young, M. S. Heimbeck, H. O. Everitt, M. Pasquali, and J. Kono, "Carbon nanotube fiber terahertz polarizer," *Appl. Phys. Lett.* **108**(14), 141107 (2016).
32. L. Ren, C. L. Pint, L. G. Booshehri, W. D. Rice, X. Wang, D. J. Hilton, K. Takeya, I. Kawayama, M. Tonouchi, R. H. Hauge, and J. Kono, "Carbon nanotube terahertz polarizer," *Nano Lett.* **9**(7), 2610–2613 (2009).

33. J. Kyoung, E. Y. Jang, M. D. Lima, H. R. Park, R. O. Robles, X. Lepró, Y. H. Kim, R. H. Baughman, and D. S. Kim, "A reel-wound carbon nanotube polarizer for terahertz frequencies," *Nano Lett.* **11**(10), 4227–4231 (2011).
34. K. Aydin, V. E. Ferry, R. M. Briggs, and H. A. Atwater, "Broadband polarization-independent resonant light absorption using ultrathin plasmonic super absorbers," *Nat. Commun.* **2**(1), 517 (2011).
35. Z. F. Liu, S. Fang, F. A. Moura, J. N. Ding, N. Jiang, J. Di, M. Zhang, X. Lepró, D. S. Galvão, C. S. Haines, N. Y. Yuan, S. G. Yin, D. W. Lee, R. Wang, H. Y. Wang, W. Lv, C. Dong, R. C. Zhang, M. J. Chen, Q. Yin, Y. T. Chong, R. Zhang, X. Wang, M. D. Lima, R. Ovalle-Robles, D. Qian, H. Lu, and R. H. Baughman, "Hierarchically buckled sheath-core fibers for superelastic electronics, sensors, and muscles," *Science* **349**(6246), 400–404 (2015).
36. P. Doradla, K. Alavi, C. S. Joseph, and R. H. Giles, "Detection of colon cancer by continuous-wave terahertz polarization imaging technique," *J. Biomed. Opt.* **18**(9), 090504 (2013).
37. J. P. Martin, C. S. Joseph, and R. H. Giles, "Continuous-wave circular polarization terahertz imaging," *J. Biomed. Opt.* **21**(7), 70502 (2016).
38. D. M. Mittleman, "Twenty years of terahertz imagin," *Opt. Express* **26**(8), 9417–9431 (2018).
39. S. Katletz, M. Pflieger, H. Pühringer, M. Mikulics, N. Vieweg, O. Peters, B. Scherger, M. Scheller, M. Koch, and K. Wiesauer, "Polarization sensitive terahertz imaging: detection of birefringence and optical axis," *Opt. Express* **20**(21), 23025–23035 (2012).
40. K. Kawase, Y. Ogawa, Y. Watanabe, and H. Inoue, "Non-destructive terahertz imaging of illicit drugs using spectral fingerprints," *Opt. Express* **11**(20), 2549–2554 (2003).
41. Y. C. Shen, T. Lo, P. F. Taday, B. E. Cole, W. R. Tribe, and M. C. Kemp, "Detection and identification of explosives using terahertz pulsed spectroscopic imaging," *Appl. Phys. Lett.* **86**(24), 241116 (2005).
42. L. Liu, A. Das, and C. M. Megaridis, "Terahertz shielding of carbon nanomaterials and their composites—a review and applications," *Carbon* **69**, 1–16 (2014).
43. W. Cai, U. K. Chettiar, A. V. Kildishev, and V. M. Shalaev, "Optical cloaking with metamaterials," *Nat. Photonics* **1**(4), 224–227 (2007).
44. Z. Huang, H. Chen, Y. Huang, Z. Ge, Y. Zhou, Y. Yang, P. Xiao, J. Liang, T. Zhang, Q. Shi, G. Li, and Y. Chen, "Ultra-broadband wide-angle terahertz absorption properties of 3D graphene foam," *Adv. Funct. Mater.* **28**(2), 1704363 (2018).
45. M. Zdrojek, J. Bomba, A. Łapińska, A. Dużyńska, K. Żerańska-Chudek, J. Suszek, L. Stobiński, A. Taube, M. Sypek, and J. Judek, "Graphene-based plastic absorber for total sub-terahertz radiation shielding," *Nanoscale* **10**(28), 13426–13431 (2018).
46. X. L. Xu, P. Parkinson, K.-C. Chuang, M. B. Johnston, R. J. Nicholas, and L. M. Herz, "Dynamic terahertz polarization in single-walled carbon nanotubes," *Phys. Rev. B Condens. Matter Mater. Phys.* **82**(8), 085441 (2010).